Divergence-free Wavelets and High Order Regularization

Souleymane Kadri Harouna, Pierre Dérian, Patrick Héas, Etienne Mémin

Noname manuscript No.
(will be inserted by the editor)

Divergence-free Wavelets and High Order Regularization

S. Kadri-Harouna · P. Dérian · P. Héas · E. Mémin

Abstract Expanding on a wavelet basis the solution of an inverse problem provides several advantages. Wavelet bases yield a natural and efficient multiresolution analysis. The continuous representation of the solution with wavelets enables analytical calculation of regularization integrals over the spatial domain. By choosing differentiable wavelets, high-order derivative regularizers can be designed, either taking advantage of the wavelet differentiation properties or via the basis's mass and stiffness matrices. Moreover, differential constraints on vector solutions, such as the divergence-free constraint in physics, can be handled with biorthogonal wavelet bases. This paper illustrates these advantages in the particular case of fluid flows motion estimation. Numerical results on synthetic and real images of incompressible turbulence show that divergence-free wavelets and high-order regularizers are particularly relevant in this context.

Keywords Divergence-free wavelets · High order derivatives regularization · optic-flow estimation

1 Introduction

Prior models used to solve ill-posed inverse problems such as images restoration, surface reconstruction or optic-flow estimation often involve differential constraints or high-order derivative regularization. In particular in the context of optic-flow estimation, numerous regularization models [12, 20] involving penalization of first or second order derivatives of the estimated velocity have been proposed in order to make this estimation problem well-defined, beginning with the original work of Horn and Schunck [12]. However, although estimation of optical flow is an old and well-known problem, it still remains very challenging in the context of fluid flows [11]. Indeed, optical flow standards are in general not designed to describe the physics of complex motions occurring at small scales. Several attempts have been carried out in order to introduce some physical constraints, such as incompressibility [8,23] for solutions of Navier-Stokes equations. Those equations describe a great variety of fluid phenomena, from oceanic streams to turbulence in the wake of airplanes. Since it is difficult to design stable discretization schemes for high-order regularizers or for differential operators such as the divergence, state of the art derivatives are limited to the second-order and very few algorithms have managed to successfully impose divergence-free constraints [23].

In addition, inverse problems often involve non-linear models. Dealing with non-linearities and the multi-scale structure of motion is particularly challenging in the optic-flow context. Gaussian multiresolution frameworks [1] or combined integrated/variational formulations [10,19] have been proposed to circumvent non-linearity and achieve long range displacement estimation. However, the former solutions suffer from a weak mathematical formulation impacting estimation accuracy, while the latter provide poor results for non-textured images such as continuous scalar flows. Even worth, as these optic-flow multiresolution schemes work only at very few distinct scales without any explicit connection between scales, estimation of large scale motion is often prone to errors.

Nevertheless, on the one hand, a multiresolution optical flow scheme based on the wavelet expansion of the motion field has been introduced by Wu et al. [22] to avoid the common drawbacks of the Gaussian pyramidal multiresolution procedure and hence, to take into account large dis-

S. Kadri-Harouna, P. Dérian, P. Héas, E. Mémin
INRIA Rennes-Bretagne Atlantique, Campus universitaire de Beaulieu, 35042 Rennes Cedex, France.
E-mail: {Souleymane.Kadri_harouna, Pierre.Derian, Patrick.Heas, Etienne.Memin}@inria.fr
http://www.irisa.fr/fluminance

placements. An extension of this work reducing the algorithm complexity has recently been proposed [4]. On the other hand, divergence-free wavelets define natural bases for the solutions of the incompressible Navier-Stokes equations. By the localization of basis functions both in scale and space and by their implicit representation of divergence-free motions, these wavelets perfectly describe the vortex structures appearing at various scales of the incompressible flow. These bases have been used extensively in the simulations of the Navier-Stokes equations and the analyses of incompressible fluid flows, with good results [5,6,21]. Additionally, expanding the solution on "regular" wavelet bases enables the easy computation of high-order derivatives and regularization integrals.

This paper introduces high-order regularization and differential constraints for inverse problems, with a special focus on the optic-flow estimation problem. It extends the approaches of [4,22] by introducing divergence-free wavelet bases for the estimation of an incompressible flow from two images. The differential constraint, characterizing the physics of fluid flows, is imposed by directly estimating coefficients of the optical flow projection onto a divergence-free wavelet basis. The methodology takes also benefits of the wavelet continuous formulation to approach or compute exactly high-order regularization integrals, and avoid unstable discrete approximations of the derivatives. In addition, in order to lower algorithm complexity, efficient quasi-Newton optimization techniques based on wavelets filter banks and the tensor structure of the separable bases are proposed.

The reminder of the paper is as follows. In section 2, we recall the basic ingredients of optic-flow computation. In section 3, we perform the biorthogonal wavelet expansion of the motion field which, as we shall see, is necessary to constrain the solution to live in the divergence-free vectorial space. Two approaches for wavelet-based high-order regularization are then introduced in section 4. Numerical results performed on synthetic and real images of 2D and 3D turbulent flows are finally presented in section 5.

2 Basic Principles of Optical Flow Techniques

This section describes briefly the motion estimation problem, and in particular how it is solved on the canonical basis or on a truncated wavelet basis. The purpose here is not to compare the various approaches proposed so far.

2.1 Problem formulation

Given two images denoted $I_1(x)$ and $I_0(x)$, motion estimation aims as finding a velocity field $\mathbf{u} = (\mathbf{u}_1, \mathbf{u}_2)^T$ minimizing the *Displaced Frame Difference* (DFD) equation[1]:

$$I_1(x + \mathbf{u}(x)) - I_0(x) = 0. \tag{1}$$

Most often, the solution is obtained by minimizing an energy functional (*cost function*):

$$F_d(\mathbf{u}) = \frac{1}{2} \int_{\mathbb{R}^2} \rho \left(I_1(x + \mathbf{u}(x)) - I_0(x) \right) dx, \tag{2}$$

where ρ may be a robust penalty function. However, for the clarity of the presentation, we will consider in the following a quadratic cost. The functional to be minimized is not convex because of the non-linearity of the image function I_1. It is in addition ill-posed as it relies on a scalar constraint for a 2D vector field unknown. This so-called *aperture problem* is solved by either reducing the dimension of the solution or by regularizing the solution with some appropriate prior model.

We present hereafter strategies to deal with cases that depart significantly from a linear assumption, *i.e* large displacements. This problem occurs particularly within the context of turbulent fluid flows, where large velocity fluctuations may be observed under condition of low time-sampling frequency.

2.2 Estimation on standard basis

Incremental multiresolution strategy is a very common technique in optical flow estimation [1]. This approach consists in building a multiresolution pyramidal representation of the image sequence by successive low-pass filtering and sub-sampling. An incremental estimation based on Gauss-Newton scheme is then achieved by solving a sequence of large systems related to linearization of model (1) around the current motion estimate. A severe drawback of the method is that the incremental estimation is driven independently at each resolution level, relying on non-imbricated linearized motion-compensated models.

2.3 Estimation on truncated wavelet basis

The wavelet-based optical flow approach first introduced by Wu et al. [22] provides a natural and mathematically

[1] In the following, we will restrict ourselves to the study of DFD equation, but the approach remains valid for any other integrated data model. Indeed, for other configurations, many other brightness evolution models have been proposed in the literature to link the image intensity function to the sought velocity field [16].

consistent multiresolution estimation framework which does not face theoretically the previous limitations. This approach performs the joint estimation of the coefficients of each scalar component of optical flow $\mathbf{u}$ decomposed on a wavelet basis. This decomposition is coherent with the idea used in standard optical flow multiresolution strategy: the inner products with scaling functions are somehow analogous to the low-pass filtering, the different projections of the image onto the scaling functions multiresolution spaces form a pyramidal representation.
The main drawback of the method described in [22] is its higher computational cost, caused by the necessity to explicitly evaluate the functional Hessian.

Recently, a new wavelet-based method that overcomes this computational burden was proposed by Dérian et al. [4]. This method consists in searching the components of the motion $\mathbf{u}$ in terms of their wavelet coefficients:

$$\mathbf{u}(x) = \Phi(x)\mathbf{d} \tag{3}$$

where $\Phi(x)$ denotes the used 2D wavelet basis and $\mathbf{d}$ the vector of coefficients of the two sought motion components. Incorporating (3) in the (DFD) equation, the argument of F_d becomes $\mathbf{d}$. Setting $I_1(x, \mathbf{d}) = I_1(x + \Phi(x)\mathbf{d})$, the gradient of F_d according to this new argument reads:

$$\nabla F_d(\mathbf{d}) = \int \left[I_1(x, \mathbf{d}) - I_0(x)\right] \nabla I_1(x, \mathbf{d}) \cdot \Phi(x) dx. \tag{4}$$

As a consequence, components of the gradient $\nabla F_d(\mathbf{d})$ of the functional are simply given by the coefficients of the wavelet decomposition of the two components of gradient:

$$\left[I_1(x, \mathbf{d}) - I_0(x)\right] \nabla I_1(x, \mathbf{d}), \tag{5}$$

on the considered wavelet basis. They are easily computed using a 2D fast wavelet transform [17] with the filter bank associated to Φ. It is easy to see that the proposed coarse-to-fine estimation strategy enables to capture large displacements: at large scales, the decomposition of (5) is obtained by convolutions with the atoms of the wavelet basis having the largest support. Note that conversely to the algorithm proposed in [22], the low-complexity of gradient computation via fast wavelet transform does not restrict motion estimation to large scales and/or images of small size. A gradient descent method is used then to minimize efficiently the functional F_d. The *aperture* problem can be here jointly addressed by reducing the problem dimension with a simple basis truncation: coefficients associated to smallest scales are not estimated, so that the number of unknowns is small enough to close the inverse problem.

3 Divergence-Free Fluid Flow Estimation

Because of their localization in both space and frequency, wavelet bases constitute interesting tools for continuous fluid flows analysis. Moreover, wavelet bases can be designed to implicitly represent divergence-free motions [5].
In this section, we recall some generalities on biorthogonal wavelet bases which, as we shall see in the following, are necessary to construct divergence-free basis for motion. Then, we briefly present the construction of anisotropic divergence-free wavelet bases in $(L^2(\mathbb{R}^2))^2$.

3.1 Biorthogonal wavelet bases on real line

In this section we recall some definitions and properties of biorthogonal multiresolution analysis (BMRA) and wavelet bases that will be used in the following.

Let $(\varphi, \tilde{\varphi})$ be a pair of scaling functions of $L^2(\mathbb{R})$ that satisfy the two-scale (or *refinement*) relations [3]:

$$\varphi(x) = \sum_{k\in\mathbb{Z}} h_k \sqrt{2}\varphi(2x - k), \tag{6}$$

$$\tilde{\varphi}(x) = \sum_{k\in\mathbb{Z}} \tilde{h}_k \sqrt{2}\tilde{\varphi}(2x - k) \tag{7}$$

with $h_k, \tilde{h}_k \in \mathbb{R}$. The masks $\{h_k\}_{k\in\mathbb{Z}}$ and $\{\tilde{h}_k\}_{k\in\mathbb{Z}}$ are called scaling function filters, they are used to implement fast-wavelet transform algorithms associated to φ and $\tilde{\varphi}$, see [17]. Moreover, one can prove that the supports of $\{h_k\}_{k\in\mathbb{Z}}$ and $\{\tilde{h}_k\}_{k\in\mathbb{Z}}$ coincide with the supports of scaling functions φ and $\tilde{\varphi}$ respectively [3].

Setting for $j, k \in \mathbb{Z}$, $\varphi_{j,k} = 2^{j/2}\varphi(2^j x - k)$ and $\tilde{\varphi}_{j,k} = 2^{j/2}\tilde{\varphi}(2^j x - k)$, we say that φ and $\tilde{\varphi}$ form a biorthogonal pair if

$$\langle \varphi_{j,k}, \tilde{\varphi}_{j,k'} \rangle = \delta_{k,k'}, \quad \forall j, k, k' \in \mathbb{Z} \tag{8}$$

where $\delta_{k,k'}$ denotes the Kronecker symbol and $< ., . >$ the $L^2(\mathbb{R})$ inner product:

$$\langle \varphi_{j,k}, \tilde{\varphi}_{j,k'} \rangle := \int_{\mathbb{R}} \varphi_{j,k}(x)\tilde{\varphi}_{j,k'}(x) dx. \tag{9}$$

In the sequel, for easy reading we will only give details on the primal setting corresponding to φ. The dual construction corresponding to $\tilde{\varphi}$ follows by analogy.

Thus, for $j \in \mathbb{Z}$, defining the spaces V_j as

$$V_j = \text{span}\{\varphi_{j,k} \ : \ k \in \mathbb{Z}\}, \tag{10}$$

the refinability of scaling function defined in (6) is known to imply that the spaces V_j form a multiresolution analysis of $L^2(\mathbb{R})$:

$$V_j \subset V_{j+1}, \ \cap_{j\in\mathbb{Z}} V_j = \{0\}, \ \overline{\cup_{j\in\mathbb{Z}} V_j} = L^2(\mathbb{R}). \tag{11}$$

Moreover, if $\varphi_{j,k}$ is compactly supported it is easy to show that the family $\{\varphi_{j,k} : \ k \in \mathbb{Z}\}$ is a Riesz basis for V_j. Then, for any $\{c_k \ : \ k \in \mathbb{Z}\} \in \ell^2(\mathbb{Z})$, there exists strictly positive constants C and C' such as:

$$C'\|c_k\|_{\ell^2(\mathbb{Z})} \leq \| \sum_{k\in\mathbb{Z}} c_k \ \varphi_{j,k}\|_{L^2(\mathbb{R})} \leq C\|c_k\|_{\ell^2(\mathbb{Z})}. \tag{12}$$

Equation (12) implies the uniform stability of the family $\{\varphi_{j,k} : j, k \in \mathbb{Z}\}$ in the sens of $L^2(\mathbb{R})$ norm.

The concept of primal wavelet consists in finding complement space W_j of V_j in V_{j+1} satisfying

$$V_{j+1} = V_j \ \oplus W_j, \qquad W_j = V_{j+1} \cap (\tilde{V}_j)^{\perp}. \tag{13}$$

These spaces are called "details" spaces. They gather the missing details of the approximation spaces V_j. It is known that such spaces W_j are generated by the dilates and translates of the wavelet function ψ [3]:

$$\psi(x) = \sum_{k\in\mathbb{Z}} g_k \sqrt{2}\varphi(2x-k), \text{ with } g_k = (-1)^k \tilde{h}_{1-k} \tag{14}$$

which satisfies

$$< \tilde{\varphi}_{j,k}, \psi_{j',k'} >= 0, \ \text{ for } \ j, j', k, k' \in \mathbb{Z}. \tag{15}$$

Further, the family of wavelet $\{\psi_{j,k} \ : \ k \in \mathbb{Z}\}$ is an unconditional basis of details space W_j. For any function $f \in L^2(\mathbb{R})$, the following decomposition formula holds:

$$f = \sum_{j\in\mathbb{Z}} \mathcal{Q}_j(f), \ \ \mathcal{Q}_j(f) = \mathcal{P}_{j+1}(f) - \mathcal{P}_j(f), \tag{16}$$

with

$$\mathcal{P}_j(f) := \sum_{k\in\mathbb{Z}} \tilde{f}_k \varphi_{j,k} \ \text{ and } \ \tilde{f}_k = \langle \tilde{\varphi}_{j,k}, f \rangle. \tag{17}$$

The advantage of wavelet bases is their ability to offer sparse representation of a signal. Note that if $\tilde{\varphi}$ is exact of order $\tilde{r} \in \mathbb{N}$:

$$x^k = \sum_{k\in\mathbb{Z}} < \varphi_k, x^k > \tilde{\varphi}_k(x), \quad 0 \leq k \leq \tilde{r}-1 \tag{18}$$

one infers from (13) and (15) that the wavelet ψ has $\tilde{r}$ vanishing moments:

$$\int_{\mathbb{R}} x^k \psi(x) dx = 0, \qquad 0 \leq k \leq \tilde{r}-1. \tag{19}$$

This construction of biorthogonal wavelet bases can be extended easily to $L^2(\mathbb{R}^d)$ $(d > 1)$ in higher dimension using tensor product of the one-dimensional basis, see [17] for more explanations.

3.2 Divergence-free wavelet bases

Compactly supported divergence-free wavelet bases have been introduced first by Lemarié-Rieusset [15]. These bases are biorthogonal and their construction is based on the existence of one-dimensional *biorthogonal wavelet bases* linked by differentiation / integration (for details see [3, 15, 17]). In particular, the main ingredients needed for such a construction are the following results proved by Lemarié-Rieusset [15]:

Proposition 1
Let $(V_j^1, \tilde{V}_j^1)$ be a "regular" biorthogonal multiresolution analysis (BMRA) of $L^2(\mathbb{R})$, associated respectively to biorthogonal scaling functions $(\varphi^1, \tilde{\varphi}^1)$ and biorthogonal wavelets $(\psi^1, \tilde{\psi}^1)$. Then there exists another BMRA denoted $(V_j^0, \tilde{V}_j^0)$, associated respectively to biorthogonal scaling functions $(\varphi^0, \tilde{\varphi}^0)$ and biorthogonal wavelets $(\psi^0, \tilde{\psi}^0)$, satisfying:

$$\frac{d}{dx}\varphi^1(x) = \varphi^0(x) \ - \ \varphi^0(x-1), \ \ \psi^1(x) = 4\int_{-\infty}^{x} \psi^0 \tag{20}$$

and

$$\frac{d}{dx}\tilde{\varphi}^0(x) = \tilde{\varphi}^1(x+1) \ - \ \tilde{\varphi}^1(x), \ \ \tilde{\psi}^0(x) = -4\int_{-\infty}^{x} \tilde{\psi}^1 \tag{21}$$

From relations (20) and (21), one can derive two interesting properties of BMRAs $(V_j^1, \tilde{V}_j^1)$ and $(V_j^0, \tilde{V}_j^0)$ [15]:

Corollary 1
Let $(V_j^1, \tilde{V}_j^1)$ and $(V_j^0, \tilde{V}_j^0)$ be two BMRAs of $L^2(\mathbb{R})$ that satisfy proposition 1, then we have:

$$(i) \ \ \frac{d}{dx}V_j^1 = V_j^0 \qquad\qquad \tilde{V}_j^0 = \int_{-\infty}^{x} \tilde{V}_j^1 \tag{22}$$

and

$$(ii) \ \ \frac{d}{dx}\mathcal{P}_j^1(f) = \mathcal{P}_j^0(\frac{d}{dx}f), \ \ \frac{d}{dx}\tilde{\mathcal{P}}_j^0(f) = \tilde{\mathcal{P}}_j^1(\frac{d}{dx}f) \tag{23}$$

for $f \in H^1(\mathbb{R})$ [2].

[2] $H^1(\mathbb{R})$ denotes the classical Sobolev space:

$$\|f\|^2_{H^1(\mathbb{R})} = \int_{\mathbb{R}} (1+|\xi|^2)|\hat{f}(\xi)|^2 d\xi$$

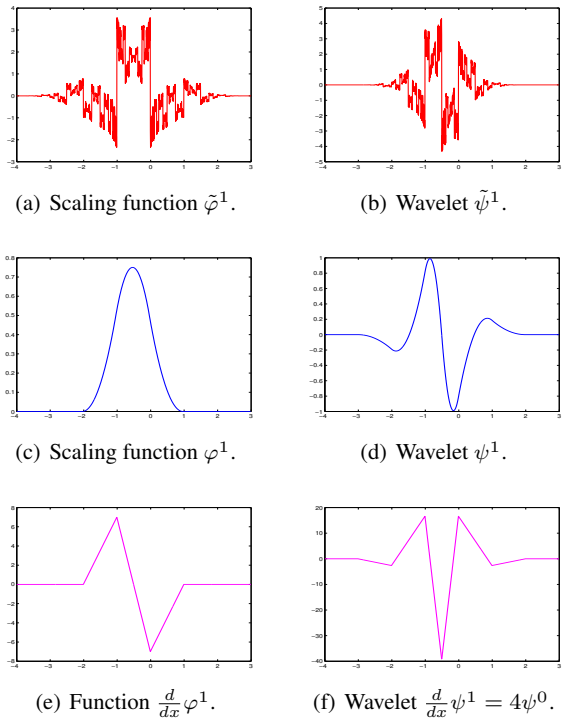

(a) Scaling function $\tilde{\varphi}^1$. (b) Wavelet $\tilde{\psi}^1$.

(c) Scaling function φ^1. (d) Wavelet ψ^1.

(e) Function $\frac{d}{dx}\varphi^1$. (f) Wavelet $\frac{d}{dx}\psi^1 = 4\psi^0$.

Fig. 1: Example of biorthogonal generators and primal derivatives: case of B-Spline generators $(\varphi^1, \tilde{\varphi}^1)$ with 3 vanishing moments.

The interest of relations (22) and (23) appears in the numerical implementation of fast divergence-free wavelet transform. These relations allow to build a multiresolution analysis of $(L^2(\mathbb{R}^2))^2$ that preserves the divergence-free property. More explanations will be given in the following. In practice, there are two types of divergence-free wavelet constructions: the isotropic construction [15] and the anisotropic one [5]. The isotropic divergence-free wavelet construction on $\mathbb{R}^d$ uses $(d-1)(2^d-1)$ types of wavelet generators with one parameter of dilatation and d parameters of translation, while the anisotropic one uses only $(d-1)$ types of wavelet generators with d parameters of dilation and translation. Thus, for $d=2$, we have one divergence-free wavelet generator in the anisotropic construction.

The objective here is to build an anisotropic wavelet basis for the divergence-free functions space $\mathcal{H}_{div}(\mathbb{R}^2)$ defined by:

$$\mathcal{H}_{div}(\mathbb{R}^2) = \{\mathbf{u} \in (L^2(\mathbb{R}^2))^2 \ : \ \nabla \cdot \mathbf{u} = 0\}. \tag{24}$$

where $\hat{f}(\xi)$ corresponds to the Fourier transform of f:

$$\hat{f}(\xi) = \int_{\mathbb{R}} f(x) e^{-i\xi \cdot x} dx$$

The space $\mathcal{H}_{div}(\mathbb{R}^2)$ can also be seen as the **curl**[3] vector potential space [7]:

$$\mathcal{H}_{div}(\mathbb{R}^2) = \{\mathbf{u} = \mathbf{curl}(\chi) \ : \ \chi \in H^1(\mathbb{R}^2)\}. \tag{25}$$

Now, to construct a wavelet basis of $\mathcal{H}_{div}(\mathbb{R}^2)$, it is natural to take the **curl** of a "*regular*" scalar multiresolution analysis of $H^1(\mathbb{R}^2)$.

At this stage, one may want to use any multiresolution analysis of $H^1(\mathbb{R}^2)$. However, let consider a "*regular*" scalar multiresolution analysis of $H^1(\mathbb{R}^2)$ generated by spaces $V_j^a \otimes V_j^b$, with $V_j^a \neq V_j^b$. Taking the **curl** of a such multiresolution analysis, we get:

$$\mathbf{curl}[V_j^a \otimes V_j^b] = \begin{vmatrix} V_j^a \otimes (V_j^b)' \\ \\ -(V_j^a)' \otimes V_j^b \end{vmatrix} \tag{26}$$

Then, to deal with the divergence-free wavelets contained in $\mathbf{curl}[V_j^a \otimes V_j^b]$, we have to manipulate four different types of biorthogonal wavelet filter banks associated respectively to the one-dimensional BMRAs that appear in (26): V_j^a, $(V_j^a)'$, V_j^b and $(V_j^b)'$. To overcome this problem, the two-dimensional scalar multiresolution analysis that we will consider is generated by

$$\mathbf{V}_j = V_j^1 \otimes V_j^1. \tag{27}$$

Using Lemarié-Rieusset's results (20) and (21), one can easily prove that:

$$\mathbf{curl}(\mathbf{V}_j) \subset \left(V_j^1 \otimes V_j^0\right) \times \left(V_j^0 \otimes V_j^1\right) = \overrightarrow{\mathbf{V}}_j. \tag{28}$$

Moreover, $\overrightarrow{\mathbf{V}}_j$ preserves the divergence-free condition:

$$\forall\, \mathbf{u} \in \mathcal{H}_{div}(\mathbb{R}^2), \ \ \nabla \cdot \overrightarrow{\mathbf{P}}_j(\mathbf{u}) = \mathbf{P}_j^0(\nabla \cdot \mathbf{u}) = 0, \tag{29}$$

with

$$\overrightarrow{\mathbf{P}}_j = \left(\mathcal{P}_j^1 \otimes \mathcal{P}_j^0\right) \times \left(\mathcal{P}_j^0 \otimes \mathcal{P}_j^1\right), \ \ \mathbf{P}_j^0 = \mathcal{P}_j^0 \otimes \mathcal{P}_j^0.$$

Accordingly, the divergence-free scaling functions spaces are defined by

$$\mathbb{V}_j^{div} = \text{span} < \Phi_{j,\mathbf{k}}^{div};\ \mathbf{k} \in \ \mathbb{Z}^2,\ j \in \ \mathbb{Z} >, \tag{30}$$

where

$$\Phi_{j,\mathbf{k}}^{div} = \mathbf{curl}[\varphi_{j,k_1}^1 \otimes \varphi_{j,k_2}^1] = \begin{vmatrix} \varphi_{j,k_1}^1 \otimes (\varphi_{j,k_2}^1)' \\ \\ -(\varphi_{j,k_1}^1)' \otimes \varphi_{j,k_2}^1 \end{vmatrix}$$

Similarly, for $\mathbf{j},\ \mathbf{k} \ \in \ \mathbb{Z}^2$, the associated anisotropic divergence-free wavelet spaces are defined by

$$\mathbb{W}_{\mathbf{j},\mathbf{k}}^{div} = \text{span} < \Psi_{\mathbf{j},\mathbf{k}}^{div};\ \mathbf{j},\ \mathbf{k} \in \ \mathbb{Z}^2 >, \tag{31}$$

[3] $\mathbf{curl}(\chi) = (\partial_y \chi, -\partial_x \chi)$.

with

$$\Psi^{div}_{\mathbf{j},\mathbf{k}} = \mathbf{curl}[\psi^1_{j_1,k_1} \otimes \psi^1_{j_1,k_2}] = \begin{vmatrix} 2^{j_2+2}\psi^1_{j_1,k_1} \otimes \psi^0_{j_2,k_2} \\ -2^{j_1+2}\psi^0_{j_1,k_1} \otimes \psi^1_{j_2,k_2} \end{vmatrix}$$

These wavelets are biorthogonal [5] and every vector field $\mathbf{u} \in \mathcal{H}_{div}(\mathbb{R}^2)$ can be decomposed uniquely as:

$$\mathbf{u} = \sum_{\mathbf{j},\ \mathbf{k} \in \mathbb{Z}^2} \langle \mathbf{u} / \tilde{\Psi}^{div}_{\mathbf{j},\mathbf{k}} \rangle \Psi^{div}_{\mathbf{j},\mathbf{k}} = \sum_{\mathbf{j},\ \mathbf{k} \in \mathbb{Z}^2} \mathbf{d}_{\mathbf{j},\mathbf{k}} \Psi^{div}_{\mathbf{j},\mathbf{k}}, \tag{32}$$

where $\langle ./. \rangle$ denotes the $(L^2(\mathbb{R}^2))^2$-inner product between two vector functions. Since $\mathbf{u}$ belongs to the multiresolution analysis formed by spaces $\overrightarrow{\mathbf{V}}_j$, its components $\mathbf{u}_1$ and $\mathbf{u}_2$ can be expanded on the two scalar wavelet bases spanned respectively by the families:

$$\{\psi^1_{j_1,k_1} \otimes \psi^0_{j_2,k_2};\ \psi^0_{j_1,k_1} \otimes \psi^1_{j_2,k_2}\},\ j_1, j_2, k_1, k_2 \in \mathbb{Z}.$$

Through an easy calculation, one shows that a renormalization of the coefficients $\mathbf{d}_{\mathbf{j},\mathbf{k}}$ yields to the coefficients of the two scalar expansions and, by identification, one can prove that the coefficients $\mathbf{d}_{\mathbf{j},\mathbf{k}}$ can be written as a linear combination of coefficients weighting the two scalar expansions [5]:

$$\mathbf{u}_1 = \sum_{\mathbf{j},\mathbf{k} \in \mathbb{Z}^2} \mathbf{d}^1_{\mathbf{j},\mathbf{k}}\ \psi^1_{j_1,k_1} \otimes \psi^0_{j_2,k_2}, \tag{33}$$

$$\mathbf{u}_2 = \sum_{\mathbf{j},\mathbf{k} \in \mathbb{Z}^2} \mathbf{d}^2_{\mathbf{j},\mathbf{k}}\ \psi^0_{j_1,k_1} \otimes \psi^1_{j_2,k_2}, \tag{34}$$

thus

$$\mathbf{d}_{\mathbf{j},\mathbf{k}} = \frac{2^{j_2+2}}{4^{j_1+2} + 4^{j_2+2}} \mathbf{d}^1_{\mathbf{j},\mathbf{k}} - \frac{2^{j_1+2}}{4^{j_1+2} + 4^{j_2+2}} \mathbf{d}^2_{\mathbf{j},\mathbf{k}}, \tag{35}$$

and

$$\mathbf{d}^1_{\mathbf{j},\mathbf{k}} = 2^{j_2+2} \mathbf{d}_{\mathbf{j},\mathbf{k}}, \qquad \mathbf{d}^2_{\mathbf{j},\mathbf{k}} = -2^{j_1+2} \mathbf{d}_{\mathbf{j},\mathbf{k}}. \tag{36}$$

Therefore, decomposition and reconstruction associated to divergence-free wavelets is simply performed using scalar wavelet filter banks. Finally, the algorithm is of low complexity and its structure remains identical to the scalar case.

We now turn to the use of such bases for fluid motion estimation issue.

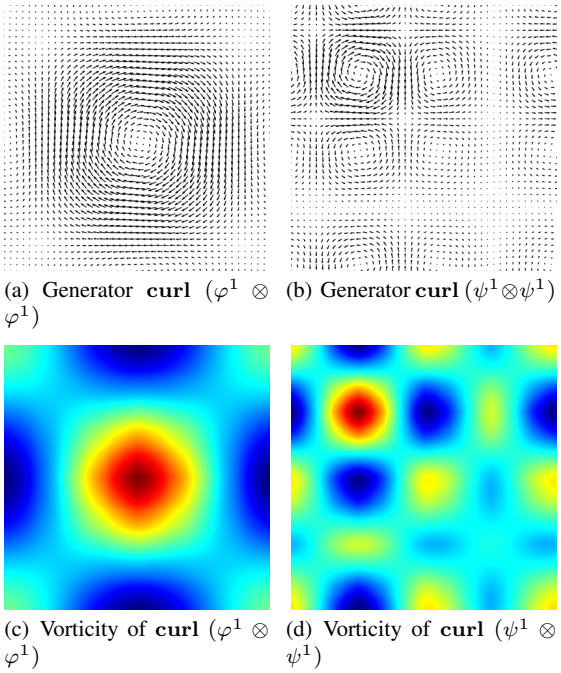

(a) Generator $\mathbf{curl}$ $(\varphi^1 \otimes \varphi^1)$ (b) Generator $\mathbf{curl}$ $(\psi^1 \otimes \psi^1)$

(c) Vorticity of $\mathbf{curl}$ $(\varphi^1 \otimes \varphi^1)$ (d) Vorticity of $\mathbf{curl}$ $(\psi^1 \otimes \psi^1)$

Fig. 2: Vector fields of divergence-free scaling functions and wavelets generators constructed from Coifflet φ^1 and ψ^1 with $r = 10$.

3.3 Divergence-free wavelet-based method

The estimation method developed in this section provides a solution to the optical flow estimation problem subject to a divergence-free constraint. The proposed approach falls within the context of wavelet-based multiresolution methods [4] sketched in the previous section. Then, the velocity field $\mathbf{u}$ is searched in terms of its divergence-free wavelet projection (32)

$$\mathbf{u}(x) = \sum_{\mathbf{j},\mathbf{k} \in \mathbb{Z}^2} \mathbf{d}_{\mathbf{j},\mathbf{k}} \Psi^{div}_{\mathbf{j},\mathbf{k}}(x), \tag{37}$$

and its estimation is reduced to the estimation of its divergence-free wavelet coefficients. Let us adopt the notation:

$$\tilde{I}_1(x, \mathbf{d}) = I_1(x + \sum_{\mathbf{j},\mathbf{k}} \mathbf{d}_{\mathbf{j},\mathbf{k}} \Psi^{div}_{\mathbf{j},\mathbf{k}}(x)).$$

The coefficients are hence defined as the minimizers of the objective function:

$$F_d(\mathbf{d}) = \frac{1}{2} \int_{\mathbb{R}^2} \left[\tilde{I}_1(x, \mathbf{d}) - I_0(x) \right]^2 dx, \tag{38}$$

where $\mathbf{d}$ is now defined as the set of the divergence-free wavelets coefficients $\{\mathbf{d}_{\mathbf{j},\mathbf{k}}\}$. Optimization is carried out by a quasi-Newton method (LBFGS), where a BFGS approximation of the Hessian relying solely on the current gradient is handled. The optimal gradient step is in addition given

in the sense of the strong Wolf conditions [18]. Obviously, besides the evaluation of the functional F_d, the descent optimization algorithm requires the computation of its gradient at each iteration step. These computations also are facilitated by the wavelet formulation. As a matter of fact, we get immediately:

$$\partial_{\mathbf{d_{j,k}}} F_d(\mathbf{d}) = \int_{\mathbb{R}^2} [\tilde{I}_1(x,\mathbf{d}) - I_0(x)] \nabla \tilde{I}_1(x,\mathbf{d}) \cdot \Psi^{div}_{\mathbf{j,k}}(x) dx$$

where

$$\begin{aligned} \nabla \tilde{I}_1(x,\mathbf{d}) \cdot \Psi^{div}_{\mathbf{j,k}}(x) \;=\; & 2^{j_2+2} \partial_{x_1} \tilde{I}_1(x,\mathbf{d}) \psi^1_{j_1,k_1} \otimes \psi^0_{j_2,k_2} \\ & - 2^{j_1+2} \partial_{x_2} \tilde{I}_1(x,\mathbf{d}) \psi^0_{j_1,k_1} \otimes \psi^1_{j_2,k_2} \end{aligned}$$

The computation of $\partial_{\mathbf{d_{j,k}}} F_d(\mathbf{d})$ thus reduces to a simple linear combination of two sets of scalar coefficients obtained by fast wavelet transforms [17]: the scalar wavelet coefficients of $[\tilde{I}_1(x,\mathbf{d}) - I_0(x)]\partial_{x_1}\tilde{I}_1(x,\mathbf{d})$, in the basis generated by $\psi^1_{j_1,k_1} \otimes \psi^0_{j_2,k_2}$, and those of $[\tilde{I}_1(x,\mathbf{d}) - I_0(x)]\partial_{x_2}\tilde{I}_1(x,\mathbf{d})$, in the basis generated by $\psi^0_{j_1,k_1} \otimes \psi^1_{j_2,k_2}$.

Remark 1
The coefficients used in the computation of $\partial_{\mathbf{d_{j,k}}} F_d(\mathbf{d})$ correspond to the dual scalar wavelet bases. To be more precise, according to (17), coefficients

$$\int_{\mathbb{R}^2} [\tilde{I}_1(x,\mathbf{d}) - I_0(x)] \partial_{x_1} \tilde{I}_1(x,\mathbf{d}) \psi^1_{j_1,k_1} \otimes \psi^0_{j_2,k_2} dx \quad (39)$$

correspond to the decomposition of

$$[\tilde{I}_1(x,\mathbf{d}) - I_0(x)] \partial_{x_1} \tilde{I}_1(x,\mathbf{d}) \quad (40)$$

on the scalar basis $\{\tilde{\psi}^1_{j_1,k_1} \otimes \tilde{\psi}^0_{j_2,k_2}\}$ and

$$\int_{\mathbb{R}^2} [\tilde{I}_1(x,\mathbf{d}) - I_0(x)] \partial_{x_2} \tilde{I}_1(x,\mathbf{d}) \psi^0_{j_1,k_1} \otimes \psi^1_{j_2,k_2} dx \quad (41)$$

correspond to the decomposition of

$$[\tilde{I}_1(x,\mathbf{d}) - I_0(x)] \partial_{x_2} \tilde{I}_1(x,\mathbf{d}) \quad (42)$$

on the scalar basis $\{\tilde{\psi}^0_{j_1,k_1} \otimes \tilde{\psi}^1_{j_2,k_2}\}$.

4 High-Order Regularization

As mentioned earlier equation (1) is a scalar constraint involving two unknowns $\mathbf{u}_1$ and $\mathbf{u}_2$ which makes the minimization of the objective function (38) an ill-conditionned problem. Truncating at small scales the wavelet expansion of $\mathbf{u}$ is a simple and direct approach yielding to interesting coarse scale polynomial approximations of the solution [4]. Nevertheless, in the context of fluid flows, the accurate estimation of small scale motion constitutes a crucial issue. A common approach is to introduce some prior knowledge on the solution regularity [12,23]. The objective of the present section is to investigate this technique in the context of standard wavelet-based method and divergence-free wavelet-based method.

To make well-conditioned the problem of optimization with the functional defined in (2), one adds a convex regularization term F_r. The objective function F_d given by (2) is then replaced by the following:

$$F(\mathbf{u}) = F_d(\mathbf{u}) + \gamma F_r(\mathbf{u}) \quad (43)$$

with the parameter $\gamma > 0$ that balances data and regularization terms.

In the following, we focus on three different high-order regularizers terms $F_r(\mathbf{u})$. Some of them have proven to be particularly adapted to fluid flows [11]. They are all based on the quadratic penalization of high-order derivatives.
A first possibility is to penalize discrepancies of the velocity field in each direction from a polynomial of degree n (i.e penalize derivative of order $n \in \mathbb{N}^*$):

$$F_r(\mathbf{u}) = \int_{\mathbb{R}^2} \sum_{\substack{1 \le i \le 2 \\ 1 \le \ell \le 2}} \left| \partial^n_{x_i} \mathbf{u}_\ell(x) \right|^2 dx. \quad (44)$$

Other approaches consist in favoring coherent vortex blobs by a second-order **curl** regularization:

$$F_r(\mathbf{u}) = \int_{\mathbb{R}^2} \left| \nabla (\partial_{x_2} \mathbf{u}_1(x) - \partial_{x_1} \mathbf{u}_2(x)) \right|^2 dx, \quad (45)$$

or approaching solutions of the heat equation:

$$F_r(\mathbf{u}) = \int_{\mathbb{R}^2} \sum_{1 \le \ell \le 2} \left| \Delta \mathbf{u}_\ell(x) \right|^2 dx. \quad (46)$$

One can notice that regularizers (45) and (46) become identical in the case of divergence-free flows. Indeed, according to [7], there exist stream function χ such as:

$$\mathbf{u} = \mathbf{curl}\ \chi, \;\; \text{with} \;\; \chi \in H^1(\mathbb{R}^2) \quad (47)$$

From the definition of "curl" operator in 2D, one can prove that:

$$-\Delta\chi = \mathbf{curl}\ (\mathbf{u}) \quad (48)$$

and this implies:

$$\left| \nabla \mathbf{curl}\ (\mathbf{u}) \right|^2 = \left| -\nabla \Delta \chi \right|^2 = \left| \partial_{x_1} \Delta \chi \right|^2 + \left| \partial_{x_2} \Delta \chi \right|^2 \quad (49)$$

Using again equation (47), we obtain:

$$\left| \Delta(\mathbf{u}) \right|^2 = \left| \Delta(\mathbf{curl}\ \chi) \right|^2 = \left| \partial_{x_1} \Delta \chi \right|^2 + \left| \partial_{x_2} \Delta \chi \right|^2 \quad (50)$$

In most cases, the operators of differentiation that appear in the previous regularizers are evaluated using finite differences methods. This creates numerical instability due to lack of precision.

The wavelet context offers an ideal setting to make such computation accurately with less effort. In the following we present two different wavelet-based schemes for high-order regularization of inverse problems. Both regularization schemes do not rely on any discrete approximation of spatial derivatives. The first approach, which is described in section 4.1, is a discrete approximation of regularization integrals. It presents the advantage to be intrinsically very simple since regularization is achieved by penalization of a subset of wavelet coefficients. The second scheme, which is described in section 4.2, constitutes a very interesting approach since it enables the exact computation of continuous regularization integrals without much more effort.

4.1 Discrete operator approximation method

In this section we describe the discrete approximation of the high-order regularization integral (44) we proposed. We show in the following that regularization can be simply expressed as the penalization of a finite set of wavelet coefficients of the motion field components.

The method is based upon differentiation properties of wavelets, deriving from the following result [17].

Proposition 2
A wavelet $\psi \in L^2(\mathbb{R})$ with a fast decay has r vanishing moments if and only if there exists θ with a fast decay such that:

$$\psi(x) = (-1)^n \frac{d^r \theta(x)}{dx^r}. \tag{51}$$

As a consequence

$$\langle f(x), \psi_{j,k}(x) \rangle = (2^{-j})^n \frac{d^r}{dx^r}(f \star \bar{\theta}_j)(x)\ , \tag{52}$$

with $\bar{\theta}_j(x) = \frac{1}{(2^{-j})^{1/2}} \theta(\frac{-t}{2^{-j}})$ and where $\star$ denotes the convolution operator. Moreover, ψ has no more than n vanishing moments if and only if $K = \int \theta(x)dx \neq 0$.

From this proposition, one can derive some interesting properties relating small scale coefficients to the function derivatives.

Corollary 2
Given a signal $f \in \mathcal{C}^n$, small scale coefficients resulting from an n-vanishing moment wavelet decomposition are related to its n^{th} derivative in the neighborhood of x:

$$\begin{aligned} \lim_{j\to\infty} \frac{\langle f(x), \psi_{j,k}(x) \rangle}{2^{-j(n+\frac{1}{2})}} &= \lim_{j\to\infty} \frac{d^n f(x)}{dx^n} \star \frac{1}{2^{-j/2}} \bar{\theta}_j(x) \\ &= K \frac{d^n f(x)}{dx^n}\ . \end{aligned} \tag{53}$$

This result can be extended to the case of 2D signals.

The penalization of small scale coefficients' amplitude thus enables to control the amplitude of the derivative of the estimated signal. Therefore, considering a finite subset $\Omega \subset \mathbb{R}^2$ defined by the set of points of a uniform grid of mesh size δx, the continuous integral defined in (44) is approximated by:

$$F_r(\mathbf{u}) \approx \delta x^2 \sum_{x\in\Omega} \sum_{\substack{1\leq i\leq 2 \\ 1\leq \ell\leq 2}} \left|\partial^n_{x_i} \mathbf{u}_\ell(x)\right|^2 + O(\delta x^2) \tag{54}$$

Considering now isotropic wavelet bases, we chose to control derivatives of motion components in the neighborhood of points in Ω, which is defined as the set of translation at the finest scale of the dyadic discrete wavelet decomposition. Approaching the limit in (53) by the smallest scale of the decomposition, we obtain:

$$F_r(\mathbf{d}) \propto \mathbf{d}^T \Lambda_{j_{max}} \mathbf{d}, \tag{55}$$

where $\Lambda_{j_{max}}$ is a diagonal matrix, whose diagonal has either zero or unitary entries in order to select coefficients $\mathbf{d}$ which are relevant of small horizontal or vertical scales.

However, due to the dyadic nature of the decomposition, only a "piecewise" control of derivatives is possible in the neighborhood of the center of translated wavelet supports. In order to control the derivative at junctions of those dyadic blocks, we redefine the set Ω, by adding points of a grid shifted by half of the smallest scale dyadic translation. To evaluate (54), we now need to compute an interpolation $\mathbf{u}_{j+1}$ of the velocity field $\mathbf{u}$ at points of this shifted grid. A multiscale interpolation scheme is used for that purpose. This operation is defined as the projection of a signal f defined at a given resolution 2^j onto the next finer approximation space V_{j+1}:

$$\check{P}_{j+1} f(2x+1) = \sum_{k=-\infty}^{+\infty} f(2k) I_{\varphi_{j+1}}(x-k+1/2) \tag{56}$$

In the case of orthogonal wavelet basis, interpolation function is defined as the autocorrelation of the scaling function φ:

$$I_{\varphi_{j+1}} = \varphi_{j+1} \star \bar{\varphi}_{j+1} \tag{57}$$

where symbol $\bar{\cdot}$ denotes the time reversed operator: $\bar{\varphi}(x) = \varphi(-x)$.

It can be shown that, this autocorrelation function interpolates exactly polynomials of order n if and only if the wavelet associated to scaling function ϕ has $n+1$ vanishing moments [17]. This linear interpolation operator $\check{P}_{j+1}$ is implemented with filter banks using filter $\check{h}$,

where $\check{h}_k = \left(h \star \bar{h}\right)_{2k+1}$ and h is defined in (6). "Interpolated coefficients" $\check{\mathbf{d}}$ are expressed as a linear combination of $\mathbf{d}$ through wavelet decomposition (resp. reconstruction) operator noted Φ (resp. $\Phi^{-1} = \tilde{\Phi}$) and interpolation: $\check{\mathbf{d}} = \left(\tilde{\Phi} \circ \check{P}_{j+1} \circ \Phi\right) \mathbf{d}$.

To control derivatives on dyadic blocks (and resp. at their junctions), small horizontal or vertical scale coefficients $\{\mathbf{d}_{j,\mathbf{k}}\}$ (resp. $\{\check{\mathbf{d}}_{j,\mathbf{k}}\}$) given by the decomposition of $\mathbf{u}$ (resp. $\check{\mathbf{u}}$) are both penalized. We finally get the regularizer

$$F_r(\mathbf{d}) \propto (\mathbf{d} + \check{\mathbf{d}})^T \Lambda_{j_{max}} (\mathbf{d} + \check{\mathbf{d}}), \tag{58}$$

and its gradient is null excepted for $j = j_{max}$:

$$\partial_{\mathbf{d}_{j,\mathbf{k}}} F_r(\mathbf{d}) = \begin{cases} \mathbf{d}_{j_{max},\mathbf{k}} + \left(\tilde{\Phi} \circ \check{P}_{j+1} \circ \Phi\right)^T \Lambda_{j_{max}} \left(\tilde{\Phi} \circ \check{P}_{j+1} \circ \Phi\right) \mathbf{d}, \\ 0 \qquad \text{for} \qquad j < j_{max}. \end{cases} \tag{59}$$

The gradient in (59) is a linear form which can be efficiently computed using recursive filter banks. The addition of the regularization term (59) therefore does not increase significantly the computational burden.

4.2 Continuous operator approximation method

The great advantage brought by the continuous optical flow representation with a finite set of coefficients of sufficiently *"regular"* wavelets, is that computation is done on the basis functions. More precisely, it enables the exact calculation of continuous spatial derivatives appearing in F_r, and the exact computation of the integrals and their gradients. This becomes possible since one knows how to compute exactly the elements of mass and stiffness matrices of compactly supported wavelet basis. To this end, we use the following results proved by Beylkin [2]:

Proposition 3
Let $\varphi \in L^2(\mathbb{R})$ be a scaling function. The function I_φ of its autocorrelation at a point x defined by:

$$I_\varphi(x) = \int_{\mathbb{R}} \varphi(y)\varphi(y - x)dy \tag{60}$$

satisfies a two scales relation:

$$I_\varphi(x) = \sum_{k \in \mathbb{Z}} i_k I_\varphi(2x - k) \tag{61}$$

where

$$i_k = \sum_{\ell \in \mathbb{Z}} h_\ell h_{\ell - k} \tag{62}$$

Similarly, the function J_φ of the correlation of φ and its derivative of order n at a point x, defined by:

$$J_\varphi(x) = \int_{\mathbb{R}} \varphi(y)\varphi^{(n)}(y - x)dy \tag{63}$$

also satisfies a two scales relation:

$$J_\varphi(x) = \sum_{k \in \mathbb{Z}} j_k J_\varphi(2x - k), \;\; \textit{with} \;\; j_k = 2^n i_k \tag{64}$$

Moreover, values of J_φ on integer points verify:

$$\sum_{\ell \in \mathbb{Z}} \ell^n J_\varphi(\ell) = (-1)^n n!. \tag{65}$$

By proposition 3, the inner products of the form $< \varphi_{j,k}, \varphi_{j,k'} >$ and $< \varphi^{(n)}_{j,k}, \varphi^{(n)}_{j,k'} >$ are eigenvectors of the matrices of terms i_k and j_k respectively. In practice, these terms are computed by solving an eigenvalue problem if the scaling function $\varphi \in L^2(\mathbb{R})$ is compactly supported [14]. To get the wavelet inner products $< \psi_{j,k}, \psi_{j,k'} >$ or $< \psi^{(n)}_{j,k}, \psi^{(n)}_{j,k'} >$, it suffices to use the two scales relation satisfied by the wavelet ψ to return to the scaling function basis.

Once we can compute the mass matrix and stiffness matrix of a wavelet basis, the computation of the regularization term F_r becomes easy. In order to clarify these points, let us explicit the computation of the term $\int_{\mathbb{R}^2} \left|\partial^n_{x_1} \mathbf{u}_1\right|^2 dx$ in the case of anisotropic divergence-free wavelet-based method, the other terms being treated similarly. From the definition of the divergence-free wavelets, we obtain:

$$\mathbf{u}_1 = \sum_{\mathbf{j},\mathbf{k} \in \mathbb{Z}^2} 2^{j_2+2} \mathbf{d}_{\mathbf{j},\mathbf{k}} \psi^1_{j_1,k_1} \otimes \psi^0_{j_2,k_2} \tag{66}$$

Thus

$$\partial^n_{x_1} \mathbf{u}_1 = \sum_{\mathbf{j},\mathbf{k} \in \mathbb{Z}^2} 2^{j_2+2} \mathbf{d}_{\mathbf{j},\mathbf{k}} \partial^n_{x_1} \psi^1_{j_1,k_1} \otimes \psi^0_{j_2,k_2} \tag{67}$$

and

$$\int_{\mathbb{R}^2} \left|\partial^n_{x_1} \mathbf{u}_1\right|^2 dx = \int_{\mathbb{R}^2} \partial^n_{x_1} \mathbf{u}_1 \cdot \partial^n_{x_1} \mathbf{u}_1 dx \tag{68}$$

$$= \sum \mathbf{d}_{\mathbf{j},\mathbf{k}} \mathbf{d}_{\mathbf{j}',\mathbf{k}'} \mathbf{R}^{j_1,j'_1}_{k_1,k'_1} \mathbf{M}^{j_2,j'_2}_{k_2,k'_2} \tag{69}$$

where $\mathbf{M}$ and $\mathbf{R}$ are respectively the one dimensional mass and stiffness matrices of the basis $\{\psi^0_{j,k}\}$ and $\{\psi^1_{j,k}\}$. Accordingly, their coefficients are given by:

$$\mathbf{M}^{j_2,j'_2}_{k_2,k'_2} = 2^{j_2+j'_2+4} \langle \psi^0_{j_2,k_2}, \psi^0_{j'_2,k'_2} \rangle$$

$$\mathbf{R}^{j_1,j'_1}_{k_1,k'_1} = \langle \partial^n_x \psi^1_{j_1,k_1}, \partial^n_x \psi^1_{j'_1,k'_1} \rangle$$

As (68) is a quadratic form, its gradient is simply given by:

$$\partial_{\mathbf{d}_{\mathbf{j},\mathbf{k}}} \int_{\mathbb{R}^2} \left|\partial^n_{x_1} \mathbf{u}_1\right|^2 dx = \sum_{\mathbf{j}',\mathbf{k}' \in \mathbb{Z}^2} \mathbf{d}_{\mathbf{j}',\mathbf{k}'} \mathbf{R}^{j_1,j_1'}_{k_1,k_1'} \mathbf{M}^{j_2,j_2'}_{k_2,k_2'} \tag{70}$$

To compute the regularization term, we use the tensor structure of the basis, unlike [22] where the two-dimensional basis functions are used. This allows us avoiding the calculation and storage of a large matrix, hence reducing the complexity of the algorithm:

$$[\partial_{\mathbf{d}_{\mathbf{j},\mathbf{k}}} \int_{\mathbb{R}^2} \left|\partial^n_{x_1} \mathbf{u}_1\right|^2 dx] = \mathbf{R}[\mathbf{d}_{\mathbf{j},\mathbf{k}}]\mathbf{M}$$

In addition, the computation of these matrices is done once for all on the scaling functions basis. To come back to the wavelet basis it suffices to use one-dimensional fast wavelet transform (FWT) on each row and column. The complexity of this transformation is $O(N)$ [17], where $N = 2^j$ and $j \in \mathbb{N}^*$ denoting the maximal one dimensional resolution. Thus the theoretical complexity of this gradient computation is at most $O(N^3)$, which is much lower than the $O(N^6)$ complexity of [22].

5 Numerical Results

5.1 Synthetic Images of Turbulence

In this section, the quality of optical flow estimation is evaluated on two different synthetic image sequences: Particle Imagery Velocimetry (PIV) images and images of an advected and diffused passive scalar. Both sequences depict the same bi-dimensional incompressible turbulent flow. The dynamic of the fluid flow is given by numerical simulation of 2D incompressible Navier-Stokes equations at $Re = 3000$, using the vorticity conservation equation and the Lagrangian equation for non-heavy particles transported by the flow (simulation details can be found in [9]). Since this simulated flow is divergence-free by construction, we can evaluate the efficiency of introducing this constraint in the wavelet bases. Image size is 256×256 pixels and the pixel grey levels have been normalized; examples of input images $I_0(x)$ from PIV and scalar sequences are displayed in Fig. 4, together with their associated ground truth motion vorticity. Estimated velocity fields are evaluated based on the Root Mean Squared end-point Error (RMSE). We will also compare and focus on vorticity fields computed from estimated motions: they exhibit the subtile differences between two different velocity estimates, and the quality of the reconstruction of this quantity is of important matter when dealing with fluid motion.

On Fig.3, we show the plot of a time-sequence of RMSE obtained by some state-of-the-art estimators, and compare it to the proposed methods:

- estimation on a truncated wavelet basis [4], using standard (i) or divergence-free (ii) wavelets;
- estimation on a divergence-free wavelet basis, using discrete (iii) or continous (iv) regularization.

The divergence-free wavelet generator ψ^1 (cases ii, iii, iv) was the Coiflet [17] with 10 vanishing moments. Since the derivative of a Coiflet is no longer an interpolating function, interpolating property for divergence-free wavelet bases is preserved in one direction by component. This same Coiflet-10 was used for the standard estimation on truncated basis (case i) for comparison. The use of 10 vanishing moments also leads to $n = 10$ order derivatives regularization (case iii) approximated by the discrete operator of section 4.1, with $\gamma = 5.10^7$ for the PIV images sequence and $\gamma = 1.10^6$ for the scalar images sequence. The Laplacian regularization (45)[4], approximated with the continuous operators as in section 4.2 was used in case (iv). The regularization parameters are $\gamma = 2.10^{-7}$ for the PIV images and $\gamma = 10^{-6}$ for the scalar images. Regarding PIV imagery, Fig. 3(a)) shows that the use of a divergence-free wavelet basis yields a significant improvement, compared to standard wavelet basis or other state-of-the-art estimators. The addition of, either the discrete or the continuous proposed regularization, enables to further outperform state-of-the-art results. Results on scalar imagery (Fig. 3(b)) show that the combination of a divergence-free wavelet basis and continuous operator regularization is necessary, in order to obtain results comparable to those of state-of-the-art. Let us note that the self-similar regularization approach proposed in [8] is probably the most accurate here since it takes advantage of an additional physical constraint. Figures 5 and 6 present vorticity fields computed from estimated motions, as well as velocity end-point error maps. On particle imagery, improvements brought by divergence-free bases (cases i, ii) are clearly visible on error maps (Fig. 5(b) and 5(d)); only smallest structures remain unestimated. The use of Laplacian regularization instead of derivative penalization (cases iii, iv) also leads to better-looking vorticity structures (Fig. 5(e) and 5(g)). This is confirmed by results on scalar imagery Fig. 6.

5.2 Experimental Turbulent Image Sequences

This section presents results obtained with real images. In order to study quasi-2D or 3D turbulent flows, the use of 2D experimental images is very common in fluid mechanics laboratories. However, traditional motion estimators usually fail or exhibit strong inaccuracy at some places.

[4] equivalent to gradient of curl regularization (46) in this context.

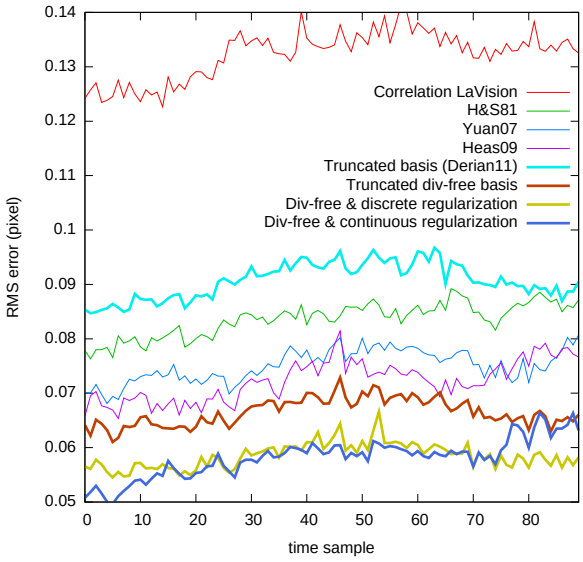

(a) Particles images

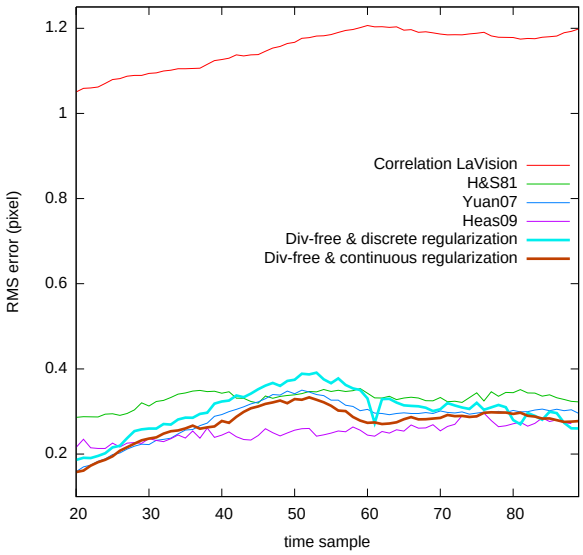

(b) Scalar images

Fig. 3: Comparison of the RMSE between proposed methods (bold lines) and some works of literature [12,23,8]. *Top*: from particle images, using truncated basis with usual (case (i), cyan) or divergence-free (case (ii), brown) wavelets, divergence-free basis with discrete (case (iii), olive green) or continuous (case (iv), dark blue) regularization operators. *Bottom:* from scalar imagery, using divergence-free basis with discrete (case (iii), cyan) or continuous (case (iv), brown) regularization operators.

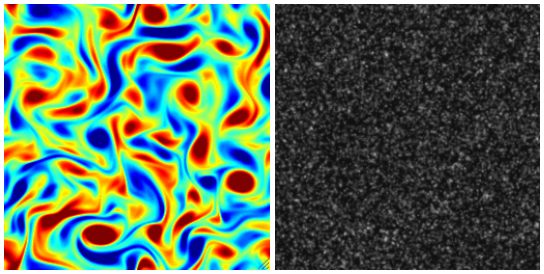

(a) True vorticity, $t = 0$ (b) First particle image $I_0(x)$

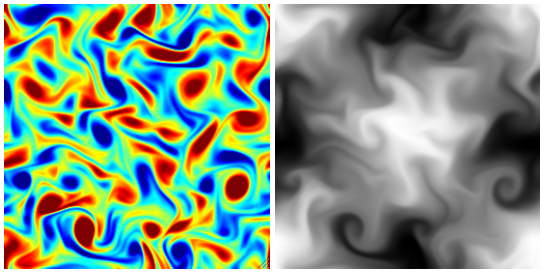

(c) True vorticity, $t = 20$ (d) First scalar image $I_0(x)$

Fig. 4: *Top:* for particle imagery, reference vorticity 4(a) and first image used 4(b), corresponding to instant $t = 0$ in sequence of Fig 3(a). *Bottom:* for scalar imagery, reference vorticity 6(a) and first image used 4(d), corresponding to instant $t = 20$ in sequence of Fig. 3(b).

The first data set consists in images of dispersion of passive tracers in a forced 2D turbulence experiment, of size 512×512 pixels [13]. The experiments were performed with electromagnetically-forced incompressible flows in stable thin stratified layers of fluid . In Fig. 7 we show an image of the sequence. For the divergence-free wavelet based-method, the employed regularizer is the same as in the case of synthetic images: continuous gradient of curl regularizer (49) (or equivalently, in this incompressible case, the Laplacian penalization) with a factor $\gamma = 2.5.10^{-8}$. For the standard wavelet based-method, we used the same regularizer model and factor, followed by a projection onto the divergence-free function space using a spectral method. Estimates show that the divergence-free wavelet based-method enables to extract more vortex structures and shear layers with better temporal continuity of the sequence; this is confirmed by the plot of the two consecutive vorticity on Fig. 8. The second real data set consists in 128 PIV pictures of a planar concomitant jet flow, of size 1024×1024 pixels. The flow is 3D and shows two high-shear regions featuring development of Kelvin-Helmholtz instabilities. Since the flow is not divergent-free, motion components are estimated on a standard scalar wavelet basis with the proposed wavelet-based gradient of curl regularizer (45), using the following settings with factor $\gamma = 10^{-7}$. Other estimates obtained with discrete second order regularization, with parameter $\gamma = 10^7$, are given for comparison. Fig. 9 presents a PIV image of the sequence and streamlines of an estimated velocity field, along with two consecutive vorticity maps computed from estimated motions, using either discrete or continuous regularization. A qualitative evaluation of estimations shows a remarkably good agreement with the physics of concomitant jets. A very good temporal coher-

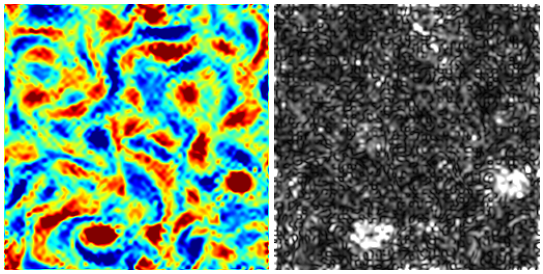

(a) Case (i) vorticity (b) RMSE $= 0.085$

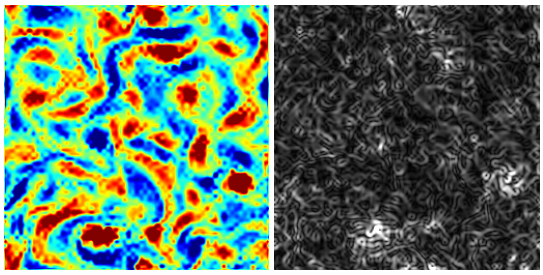

(c) Case (ii) vorticity (d) RMSE $= 0.064$

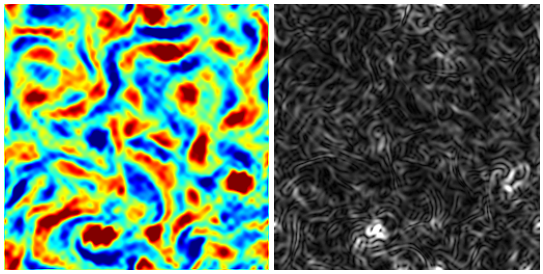

(e) Case (iii) vorticity (f) RMSE $= 0.057$

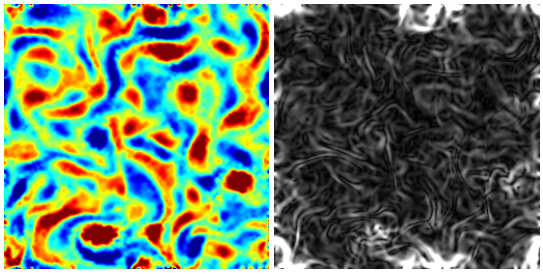

(g) Case (iv) vorticity (h) RMSE $= 0.051$

Fig. 5: *Left column*: vorticity computed from velocity fields estimated from particle imagery (Fig. 4(b)) with the 4 presented cases, to be compared with the reference Fig. 4(a). *Right column*: corresponding velocity end-point error.

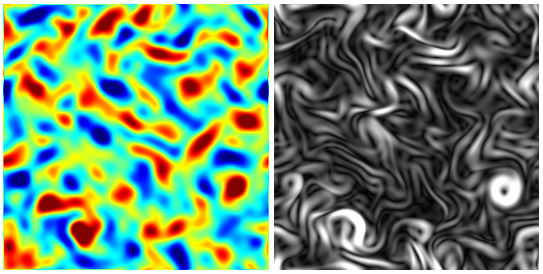

(a) Case (iii) vorticity (b) RMSE $= 0.19$

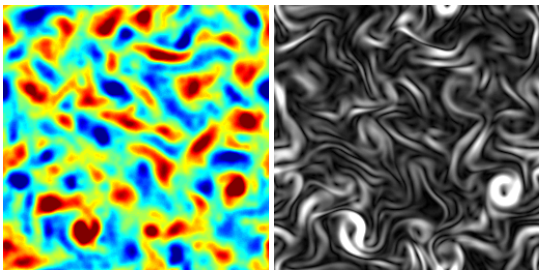

(c) Case (iv) vorticity (d) RMSE $= 0.16$

Fig. 6: *Left:* vorticity computed from velocity fields estimated from scalar imagery (Fig. 4(d)), using Div-free wavelets method and discrete (*top*) or continuous (*bottom*) regularization. *Right:* corresponding velocity end-point error.

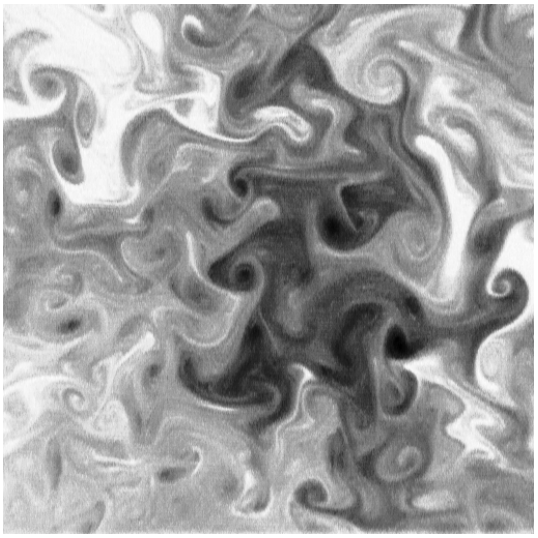

Fig. 7: Experimental image of passive scalar dispersion in a 2D turbulent motion, corresponding to time $t = 89$. This image has been normalized so as to enhance visualization.

ence is also observed, although no prior dynamic model is considered (i.e successive pairs of images are processed independently). Results obtained using continuous regularization however show the evolution of finer structures, i.e. a richer dynamic.

6 Conclusion

Based on a biorthogonal wavelet expansion of optical flow and particularly divergence-free wavelet in the incompressible case, we have proposed an algorithm dedicated to the estimation of fluid motion. The wavelet-based algorithm is of low-complexity and offers an intrinsic and efficient mul-

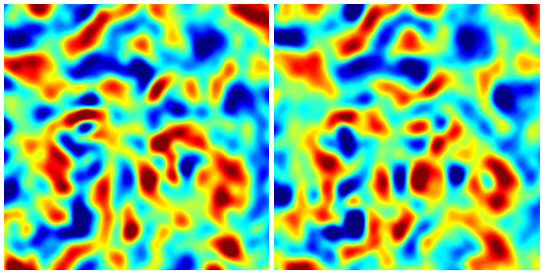

(a) Usual basis, $t = 88$. (b) Usual basis, $t = 89$.

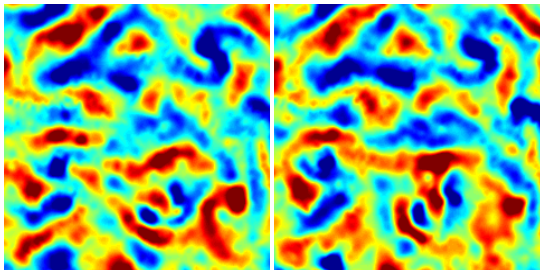

(c) Div.-free basis, $t = 88$. (d) Div.-free basis, $t = 89$.

Fig. 8: Details of two successive vorticity fields computed from estimated velocity fields, using experimental 2D scalar image dataset at $t = 88$ and $t = 89$ (input image Fig. 7). Both cases use continuous Laplacian regularization with $\gamma = 2.5.10^{-8}$, associated to usual Coiflet-10 wavelet basis (*top*) and divergence-free basis generated from same Coiflet-10 (*bottom*). Enhancement brought by the divergence-free basis is clearly visible, with much better-defined structures as well as a better temporal coherence on *bottom row* vorticity fields.

tiresolution estimation framework. Taking advantage of the continuous representation of optical flow by a finite set of wavelet coefficients, we have proposed a family of high-order regularizers designed for fluid flows. They rely on the approximation or the exact computation (without any discretization approximations in both cases) of differential operators of arbitrary order. The regularizers are approached in the first case by simply constraining small scale coefficients, while in the second case it is calculated exactly by the simple calculation of one-dimensional wavelet basis mass and stiffness matrices. Numerical results obtained with challenging particle and scalar image sequences of 2D and 3D turbulence show a significant performance enhancement compared to state of the art methods.

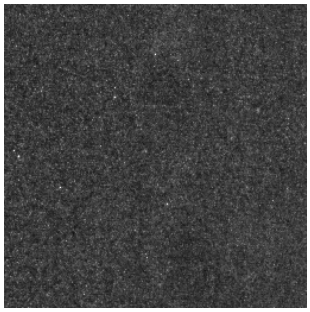

(a) First scalar image $I_0(x)$

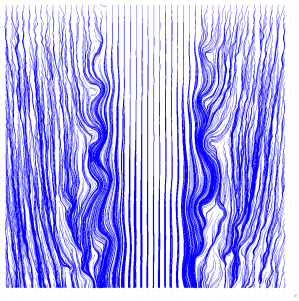

(b) Example of streamlines

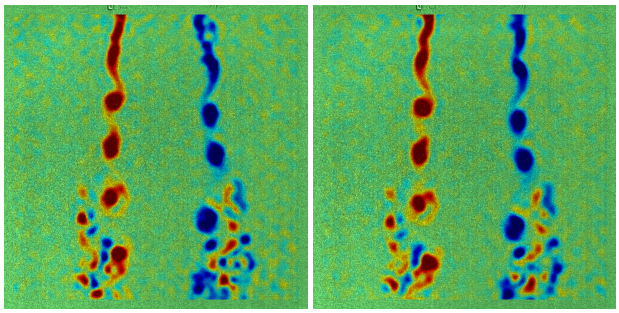

(c) Discrete regul., t=16 (d) Discrete regul., t=17

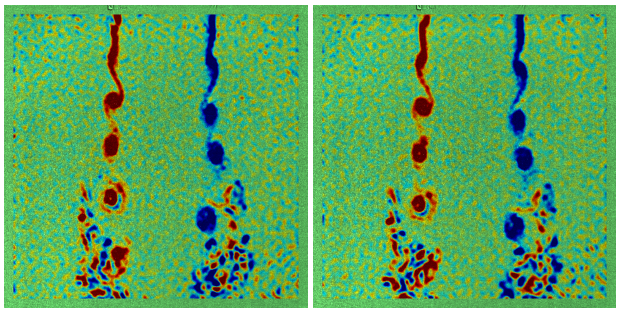

(e) Continuous regul., t=16 (f) Continuous regul., t=17

Fig. 9: Results from 2D planar jet PIV dataset. *Top:* detail of input PIV image 9(a), streamlines 9(b). *Middle:* vorticity computed from two consecutive estimated motions, using discrete regularization. *Bottom:* vorticity computed from estimations using continuous regularization.

References

1. Bergen, J., Burt, P., Hingorani, R., Peleg, S.: A 3-frame algorithm for estimating two-component image motion. IEEE Trans. Pattern Anal. Mach. Intell. **14**(9), 886–895 (1992)
2. Beylkin, G.: On the representation of operator in bases of compactly supported wavelets. SIAM J. Numer. Anal **6**(6), 1716–1740 (1992)
3. Cohen, A., Daubechies, I., Feauveau, J.C.: Bi-orthogonal bases of compactly supported wavelets. Comm. Pure Appli. Maths **45**, 485–560 (1992)
4. Dérian, P., Héas, P., Herzet, C., Mémin, E.: Wavelet-based fluid motion estimation. In: 3rd International Conference on Scale-Space and Variational Methods in Computer Vision (SSVM2011), IEEE LNCS. Ein-Gedi, Israel (2011)
5. Deriaz, E., Perrier, V.: Divergence-free and Curl-free wavelets in 2D and 3D, application to turbulence. J. of Turbulence **7**, 1–37 (2006)
6. Deriaz, E., Perrier, V.: Direct numerical simulation of turbulence using divergence-free wavelet. SIAM Multi. Mod. and Simul. **7**(3), 1101–1129 (2008)
7. Girault, V., Raviart, P.: Finite Element Methods for Navier-Stokes Equations: Theory and Algorithms. Springer Series in Computational Mathematics. Springer-Verlag. (1986)
8. Heas, P., Memin, E., Heitz, D., Mininni, P.: Bayesian selection of scaling laws for motion modeling in images. In: International Conference on Computer Vision (ICCV'09). Kyoto, Japan (2009)
9. Heitz, D., Carlier, J., Arroyo, G.: Final report on the evaluation of the tasks of the workpackage 2, FLUID project deliverable 5.4.

Tech. rep., INRIA - Cemagref (2007)
10. Heitz, D., Heas, P., Memin, E., Carlier, J.: Dynamic consistent correlation-variational approach for robust optical flow estimation. Experiments in Fluids **45**, 595–608 (2008)
11. Heitz, D., Mémin, E., Schnörr, C.: Variational fluid flow measurements from image sequences: synopsis and perspectives. Experiments in fluids **48**(3), 369–393 (2010)
12. Horn, B., Schunck, B.: Determining optical flow. Artificial Intelligence **17**, 185–203 (1981)
13. Jullien, M., Castiglione, P., Tabeling, P.: Experimental Observation of Batchelor Dispersion of Passive Tracers. Physical Review Letters **85**(17), 3636–3639 (2000)
14. Kadri-Harouna, S.: Ondelettes pour la prise en compte de conditions aux limites en turbulence incompressible (2010). Phd thesis (`in french`), Grenoble University, 2010.
15. Lemarié-Rieusset, P.: Analyses multirésolutions non orthogonales, commutation entre projecteurs et dérivation et ondelettes vecteurs à divergence nulle. Revista Matematica Iberoamericana **8**, 221–237 (1992)
16. Liu, T., Shen, L.: Fluid flow and optical flow. Journal of Fluid Mechanics **614**, 253 (2008)
17. Mallat, S.: A Wavelet Tour of Signal Processing: The Sparse Way. Academic Press (2008)
18. Nocedal, J., Wright, S.J.: Numerical Optimization. Springer Series in Operations Research. Springer-Verlag, New York, NY (1999)
19. Steinbruecker, F., Pock, T., Cremers, D.: Large displacement optical flow computation without warping. In: IEEE International Conference on Computer Vision (ICCV). Kyoto, Japan (2009)
20. Suter, D.: Motion estimation and vector splines. In: Proc. Conf. Comp. Vision Pattern Rec., pp. 939–942. Seattle, USA (1994)
21. Urban, K.: Wavelets in Numerical Simulation. Springer (2002)
22. Wu, Y., Kanade, T., Li, C., Cohn, J.: Image registration using wavelet-based motion model. Int. J. Computer Vision **38**(2), 129–152 (2000)
23. Yuan, J., Schnörr, C., Memin, E.: Discrete orthogonal decomposition and variational fluid flow estimation. Journ. of Math. Imaging & Vison **28**, 67–80 (2007)